Chuan Luo
Assistant Professor
Department of Precision Instruments,
Tsinghua University,
Beijing 100084, China

W. C. Tai
Department of Mechanical Engineering,
University of Washington,
Seattle, WA 98195-2600

Cheng-Wei Yang
Department of Mechanical and
Aerospace Engineering,
University of California, Los Angeles,
Los Angeles, CA 90095-1597

G. Z. Cao
Professor
Department of Material
Science and Engineering,
University of Washington,
Seattle, WA 98195-2120

I. Y. Shen[1]
Professor
Department of Mechanical Engineering,
University of Washington,
Box 352600,
Seattle, WA 98195-2600
e-mail: ishen@u.washington.edu

Effects of Added Mass on Lead-Zirconate-Titanate Thin-Film Microactuators in Aqueous Environments

In this paper, we conduct experimental, theoretical, and numerical studies of a lead-zirconate-titanate (PZT) thin-film microactuator probe submerged in water. The major component of the actuator is a PZT diaphragm anchored on four silicon sidewalls. There is also silicon residue at the juncture of the diaphragm and the sidewalls due to imperfect etching processes. In the experimental study, frequency response functions of actuator displacement are measured via a laser Doppler vibrometer and a spectrum analyzer. The measurements show that the first natural frequency of the microactuator reduces from 80 kHz in air to 20 kHz when the microactuator is submerged in water. A viable explanation is that the surrounding water induces significant added mass to the microactuator. Estimation of the added mass based on theories in fluid mechanics successfully reconciles the predicted frequency to the vicinity of 20 kHz confirming the effects of added mass. Finite element models are also created to study how the silicon sidewalls and residue affect the added mass. Simulations show that presence of the sidewalls or residue would modify the fluid flow thus altering the added mass and natural frequency. In general, the finite element predictions agree well with the experimental measurements within 10% difference. [DOI: 10.1115/1.4034613]

1 Introduction

Hearing loss is a common disability in aging seniors and people who work long hours in noisy environments. Severe hearing loss often results from dysfunction or loss of cochlear hair cells. For these patients, a neural prosthesis implanted in cochlea is a common strategy to treat the hearing loss.

There are two research directions regarding future implants for hearing rehabilitation. One is acoustic microactuators that generate pressure waves in cochlea. Such devices, when integrated with cochlear implant electrodes, will lead to hybrid cochlear implants [1,2] that generate electric and acoustic stimulation simultaneously to auditory nerves improving speech recognition [3–5]. The other direction is intracochlear microphones, which will eventually advance current cochlear implants into a totally implantable device [6,7].

Piezoelectric microelectromechanical systems (MEMS) devices are ideal candidates for these two applications for their small size, high sensitivity, large bandwidth, and high actuation strength. Moreover, piezoelectric materials can serve as sensors and actuators. (For a comprehensive review of piezoelectric MEMS devices, please refer to Ref. [8].) Development of piezoelectric MEMS devices for actuator applications would transplant smoothly to sensor applications, and vice versa. In designing these piezoelectric MEMS devices for intracochlear applications, one important consideration is how the aqueous environment in cochlea would affect performance of these devices.

Microelectromechanical systems devices interacting with surrounding fluid have been studied widely, in particular their squeeze-film damping effects [9,10]. This damping effect could

be critical for piezoelectric resonators, because it could significantly reduce the Q-factor thus reducing amplitude of the resonators [11,12]. In such devices, the ambient fluid is often gas (e.g., air) and the moving part defining the squeeze film is usually rigid (e.g., a proof mass). Therefore, the effect of added mass is virtually nonexistent.

In contrast, intracochlear piezoelectric microactuators or microphones face a totally different setup. First, the ambient fluid (perilymph) has a much higher density than gas. Also, the moving surface is usually flexible (e.g., a diaphragm) behaving like a speaker [1,2]. Under these conditions, the added mass could become dominant, significantly reducing the natural frequencies and bandwidth of these intracochlear microdevices.

Effects and importance of added mass are well known for macrostructures, but receive little attention for MEMS applications. In fact, there are very few papers in the MEMS literature that study effects of added mass, and one of them is by Park et al. [13]. In Ref. [13], they measure mass, stiffness, and damping of a resonant structure in deionized (DI) water, in 9% glucose solution, and in 18% glucose solution. Their experimental results show that the mass of the resonator is larger in the 18% glucose solution than in the DI water. Moreover, the mass of the resonator increases as the size of perforation in the resonator decreases. Only presence of added mass can satisfactorily explain these experimental observations. Despite these celebrated measurements, Park et al. [13] did not predict the added mass theoretically or calculate it numerically to confirm their experimental measurements. Obviously, the knowledge base of added mass for MEMS applications needs to be broadened.

Although the added mass is a classic phenomenon observed in many naval structures, how it would affect performance of an MEMS device is largely not understood due to unique aspect ratios of MEMS devices. In particular, thin-film structures used in MEMS devices could lead to extremely large aspect ratios. For

example, a diaphragm with a 2-μm thickness and an 800-μm span will lead to an aspect ratio of 400. Such a huge aspect ratio is not often observed in traditional naval structures. As a result, the added mass has significantly more influence on the natural frequencies for MEMS devices than for naval structures. Moreover, MEMS devices have significantly higher natural frequencies than naval structures (e.g., 80 kHz versus 2 Hz). A 50% drop of natural frequencies is much more noticeable in MEMS devices than in naval structures.

Because of the scarce of existing literature, many questions encountered in the development of intracochlear microactuators remain wide open. For example, if an intracochlear microactuator is tested in water, how will the water level affect the actuator bandwidth? When an intracochlear microactuator is implanted in cochlea, it will be confined in a very tiny duct (scala tympani), which is bounded by a soft basilar membrane and hard skull bone. In this case, how will perilymph in the duct and the soft and hard boundaries affect the added mass of the microactuator?

It is also not clear how various features of an MEMS device affect the added mass. For example, acoustic microactuators often employ rigid sidewalls to support an elastic diaphragm to generate acoustic waves. These sidewalls will certainly affect flow fields and subsequently the added mass. As another example, etching processes (e.g., deep reactive ion etch) in MEMS devices often leave behind round corners and residues. How will these features affect the added mass in the resulting MEMS devices?

The purpose of this paper is to answer some of the questions above by conducting experimental, theoretical, and numerical studies on vibration of piezoelectric MEMS devices in air and in water. We will start with a brief explanation of the piezoelectric MEMS device we have developed, i.e., an intracochlear acoustic microactuator. Then, we will discuss the natural frequencies experimentally measured from the device via a laser Doppler vibrometer and a spectrum analyzer. Dramatic changes of the natural frequency in air and in water indicate the presence of a significant added mass when the piezoelectric MEMS device is submerged in the water. In order to verify the experimental results, we conduct a literature search to identify several mathematical models to estimate the added mass and successfully reconcile the measured natural frequencies in air and in water. Finally, we conducted a thorough numerical analysis using finite element models. We further study how various parameters, such as water level, presence of sidewalls, and residual silicon, affect the added mass and bandwidth of the piezoelectric MEMS device.

2 Device Description

The piezoelectric MEMS device studied in this paper is a PZT thin-film microactuator [14]. The microactuator has a membrane structure and consists of four parts: a diaphragm, a bulk silicon substrate, a PZT thin-film layer, and a pair of electrodes (see Fig. 1). (Note that the parts in Fig. 1 are not drawn in proportion.) The
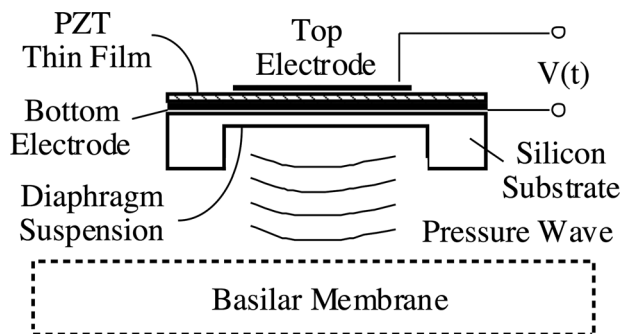
diaphragm can be formed, for example, by etching the silicon substrate from the back to form a cavity under the diaphragm.

The diaphragm is a deflecting part of the actuator anchored to the silicon substrate. As a result of its small thickness, the silicon diaphragm has low structural stiffness compared with the substrate. On top of the silicon diaphragm is a layer of PZT thin film with a pair of bottom and top electrodes. When used as an actuator, a driving voltage is applied to the electrodes extending or contracting the PZT thin film in the plane of the diaphragm, thus creating a bending moment to flex the diaphragm out of its plane. When used as a sensor, the pressure waves deform the diaphragm extending or contracting the PZT thin film to generate piezoelectric charge. Many researchers have used this configuration for design of microphones or resonators [11,12,15].

To fit the PZT thin-film microactuator into tiny space of cochlea, the diaphragm portion along with its anchor is diced off from the silicon substrate to form a PZT probe (see Fig. 2). The PZT probe is 1 mm wide, 10 mm long, and 0.4 mm thick. The PZT thin-film diaphragm (with a size of 0.8 mm × 0.8 mm) is located at the tip of the probe. The entire actuator is packaged with parylene of 0.25 μm thick together with lead wires for bottom and top electrodes of the piezoelectric diaphragm. Detail fabrication steps of this device can be found in Ref. [8].

3 Experimental Studies

Calibrated experiments are conducted to evaluate the performance of the PZT probe in air and in water. Water is chosen because its density is very similar to that of the fluid in cochlea (perilymph). Based on Ref. [16], the density of perilymph is about 1.01 g/cm^3 (1% larger than water). The viscosity of perilymph is about 2 cP (as opposed to 1 cP for water) [17]. Since the added mass significantly depends on the fluid density but not so much on fluid viscosity, the added mass effect measured in water will be reasonably close to that in perilymph. To make the experiments easy to prepare, we use water as the ambient fluid. The experimental setup and measurement results are described in detail as follows.

The PZT probe is first poled with 5 V for 10 mins and 12 V for 20 mins subsequently. A swept-sine source from a spectrum analyzer, amplified by an AVC amplifier, drives the PZT probe as an actuator. In the meantime, a laser Doppler vibrometer (LDV) measures the velocity of the center point of the PZT probe diaphragm. (Specifically, the laser spots on the top center electrode, whose gold surface reflects the laser back to LDV to detect velocity of the diaphragm.) The spectrum analyzer then processes the swept-sine driving voltage and LDV measurement to obtain a frequency response function (FRF). Finally, the FRF is converted to actuator displacement versus driving voltage in the frequency domain. The experiment is repeated with the PZT microactuator probe in air and in water. When the PZT probe is in water, we compensate the LDV measurement by using index of refraction of
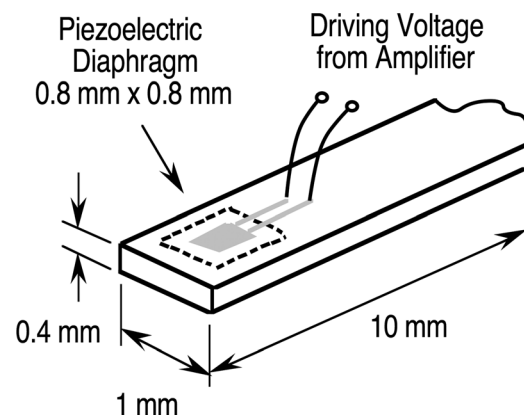

Fig. 1 Schematic drawing of PZT thin-film membrane actuator placed in cochlea (not to scale)

Fig. 2 Schematic drawing of the PZT microactuator probe

the water to obtain the correct velocity and displacement of the PZT probe diaphragm. A schematic drawing and a photo of the experimental setup are shown in Fig. 3.

As shown in Fig. 3, majority of the PZT probe is fixed and packaged with silicone. The exposed tip of the probe is less than 2 mm to mimic the situation after implantation. With such a short cantilever, the first natural frequency of the cantilever far exceeds 100 kHz [8] and is outside the range of our measurements. As a result, the LDV will only measure deflection of the diaphragm, which is most relevant to the effect of added mass.

Figure 4 compares the measured FRF in air and in water. In air, the first natural frequency of the diaphragm is around 80 kHz. In water, the first natural frequency of the diaphragm is dropped to 20 kHz. These measurements prompt many questions whose answers remain open. For example, why did the natural frequency experience such a huge drop in water? If the drop resulted from the added mass, how would we prove it? Could we predict theoretically or calculate numerically how much the natural frequency would drop given an ambient fluid? Would the cross-sectional geometry (e.g., silicon sidewalls) of the probe affect the added mass? How would the water level in the experiment affect the natural frequency?

4 Theoretical Studies

The goal of the theoretical studies is to find out what causes the huge drop in the natural frequency. We adopt the process of elimination to narrow the search.
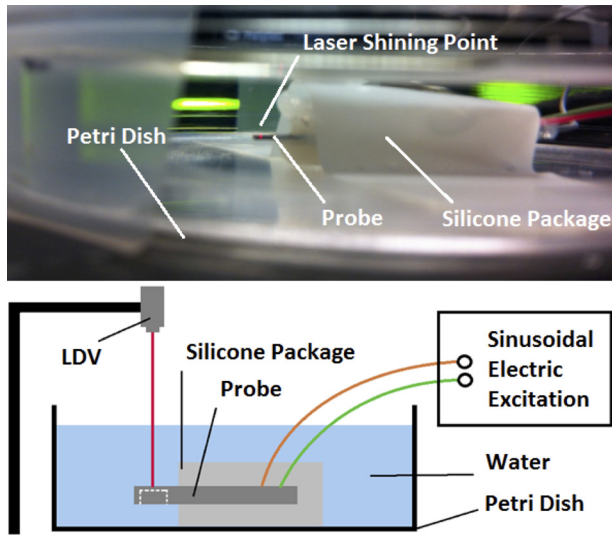

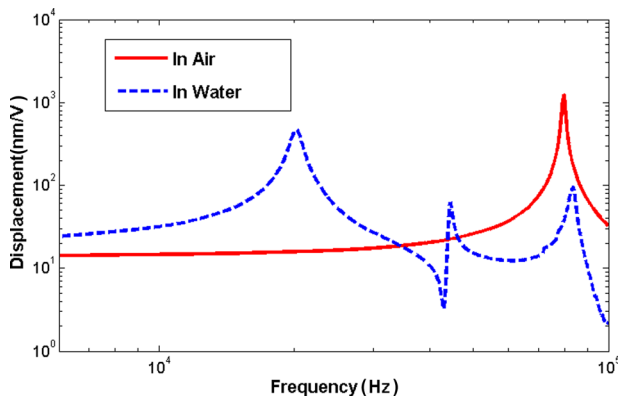**Fig. 3 Photo and schematic drawing of experimental setup**

Fig. 4 Measured FRF of the PZT probe in air and in water

First, the huge frequency drop cannot come from damping of the water. Experimentally, a viscous damping factor can be easily calculated from the measured FRF shown in Fig. 4 via the half-power method. A quick calculation shows that the viscous damping factor in air (i.e., the mode at 80 kHz) is $\zeta_{air} \approx 0.9\%$. In contrast, the viscous damping factor in water (i.e., the mode at 20 kHz) is $\zeta_{air} \approx 2.5\%$. According to vibration theories, peak amplitude of a second-order FRF from a spring–mass–damper system occurs at the frequency $\omega_{peak} = \omega_n \sqrt{1 - 2\varsigma^2}$, where ω_n is the undamped natural frequency and ζ is the viscous damping factor. When ζ changes from 0.9% to 2.5%, the shift of ω_{peak} is less than 0.05%. In contrast, the measured ω_{peak} in Fig. 4 shows a drop of 75%. It is clear that damping plays almost no role in the frequency shift in Fig. 4.

So what causes the huge drop in the first natural frequency? For a single-degree-of-freedom system, the natural frequency is $\sqrt{k/m}$. Therefore, a significant drop in the natural frequency implies a huge drop in stiffness k or a large increase in mass m. For the PZT microactuator probe in water, there is no obvious mechanism to reduce the stiffness k. There is, however, one possible mechanism to significantly increase the mass m, that is, the added mass from the surrounding water. To validate this hypothesis, we need to estimate the added mass and predict the natural frequency measured in water.

Accurate prediction of the added mass is indeed a challenging task for several reasons. First, the added mass depends not only on geometry but also on the vibration shape of the diaphragm. Second, the added mass depends on various assumptions made in the fluid mechanics that predicts pressure loading on the diaphragm. As a result, there are many mathematical models available to predict the added mass. In this paper, we follow the derivation in a review paper by Yadykin et al. [18].

Let us consider a square diaphragm shown in Fig. 5 with length l and a uniform thickness h. The diaphragm is treated as a thin plate simply supported at four edges. When the diaphragm vibrates in its first mode, the displacement field of the diaphragm is

$$w(x, y, t) = \delta(t) \sin\left(\frac{\pi x}{l}\right) \sin\left(\frac{\pi y}{l}\right) \qquad (1)$$

where $\delta(t)$ is the displacement at the center of the diaphragm. In addition, the diaphragm is submerged in an incompressible, inviscid, and stationary fluid of density ρ_f.

According to Ref. [18], the added mass m_f can be found as

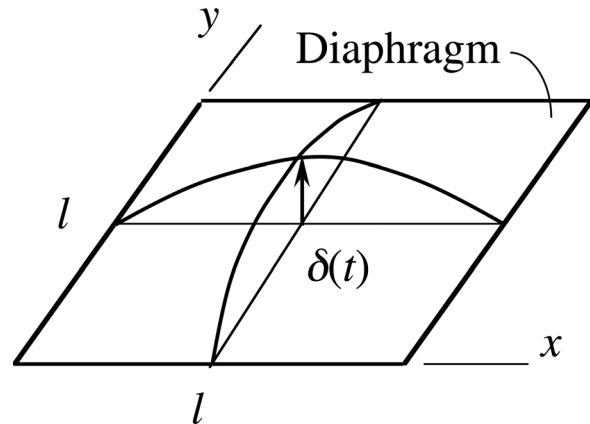$$m_f = \frac{\mu}{\pi} \rho_f l^3 \qquad (2)$$

Fig. 5 Assumed shaped for the calculation of added mass; the square domain has a simply supported boundary condition

where μ is a coefficient predicted from a fluid mechanics model. For example, $\mu \approx 2.8$ from a two-dimensional theory, $\mu \approx 2.5$ from a three-dimensional (3D) theory, $\mu \approx 2.1$ from a thin airfoil theory, and $\mu \approx 2.0$ from a traveling wave solution.

On the other hand, let us assume that the diaphragm has an average density ρ. Then, the mass of the diaphragm is

$$m = \rho l^2 h \tag{3}$$

Therefore, the ratio of the added mass to the diaphragm mass is

$$\frac{m_f}{m} = \frac{\mu}{\pi} \cdot \frac{\rho_f}{\rho} \left(\frac{l}{h} \right) \tag{4}$$

As shown in the above equation, the added mass can become quite significant if the length-to-thickness ratio of the diaphragm is large. Since natural frequencies are inversely proportional to the square root of the mass, the natural frequency in the fluid ω_f will be related to the natural frequency in the air ω_{air} through

$$\frac{\omega_f}{\omega_{air}} = \sqrt{\frac{m}{m + m_f}} = \sqrt{\frac{1}{1 + \frac{\mu}{\pi} \cdot \frac{\rho_f}{\rho} \left(\frac{l}{h} \right)}} \tag{5}$$

The above equation can be used to explain why the measured frequency drops from 80 kHz to 20 kHz as follows. First, the diaphragm consists of multiple layers of different thickness and material properties. Table 1 lists the estimated thickness and density of each layer. With diaphragm size being $0.8\,mm \times 0.8\,mm$ (i.e., $l = 800\,\mu m$), the mass of the diaphragm is $m = 1.060 \times 10^{-8}$ kg based on the estimates in Table 1. In contrast, the added mass, calculated from Eq. (2) assuming a 3D theory (i.e., $\mu \approx 2.5$), is $m_f = 4.074 \times 10^{-7}$ kg. These calculations show that the added mass is significantly larger than the diaphragm mass. With $\omega_{air} = 80$ kHz, the calculation from Eq. (5) predicts that $\omega_f = 12.7$ kHz, which is in the vicinity of the measured value of 20 kHz.

5 Discussion

The discrepancy between the theoretical prediction (i.e., 12.7 kHz) and the experimental measurement (i.e., 20 kHz) may come from several sources.

The first source is uncertainties from the fluid mechanics model used. One should note that the predicted natural frequency in water is only an estimate, because different fluid mechanics models give different predictions of the added mass. For example, if a model by Meyerhoff [19] is adopted, the predicted added mass will be given by

$$m_f = 0.579 \left(\frac{\pi}{4} \right) \rho_f l^3 \tag{6}$$

Using this mathematical model, the added mass will be $m_f = 2.328 \times 10^{-7}$ kg and the predicted frequency in the water will be

$\omega_f = 16.7$ kHz. Since the added mass is in general one order-of-magnitude larger than the diaphragm mass, a minor variation of the theoretical added mass could significantly change the predicted natural frequency in water.

Also, the fluid flow present in the experiments may be more complex than what is assumed in the fluid mechanics models. For example, Yadykin et al. [18] assume that the diaphragm is submerged in the fluid without any obstruction of the fluid flow. As far as the PZT probe in the experiments is concerned, the fluid on one side of the diaphragm is free to flow. The fluid at the other side of the diaphragm, however, is confined within the sidewalls.

The second source of discrepancy is uncertainties resulting from boundary conditions. Specifically, the boundary conditions in the probe are not identical to those in the theoretical models. In Ref. [18], a simply supported boundary condition is assumed, thus leading to a half-sine deflection in Eq. (1). The PZT diaphragm, however, is subjected to a fixed boundary condition. The difference in boundary conditions is equivalent to a reduction in the diaphragm length l, which is demonstrated as follows.

Figure 6 shows a cross-sectional view of a PZT probe made in the same batch. Note that the diaphragm near the edges does not have a uniform thickness (marked as silicon residue in Fig. 6). At the central portion of the diaphragm, the thickness is very uniform and the diaphragm behaves like a membrane. In contrast, the silicon residue at the edges provides significantly larger bending rigidity staging a fast transition to a fixed boundary condition. The presence of the silicon residue reduces the effective area of the diaphragm, over which the half-sine deflection in Eq. (1) is assumed.

Figure 7 shows a calculated deflection profile of the probe (via a finite element analysis (FEA) in Ref. [14]) of a cross section passing through the diaphragm center and parallel to the x-axis (cf. Fig. 5). The deflection is plotted over half of the diaphragm, with the center located at the origin and the edge at $400\,\mu m$. As shown in Fig. 7, the central portion of the PZT diaphragm follows the half-sine deflection in Eq. (1) quite well. For the region between $300\,\mu m$ and $400\,\mu m$, the presence of the silicon residue drastically suppresses the displacement and transitions the

Table 1 Thickness and density of layered diaphragm

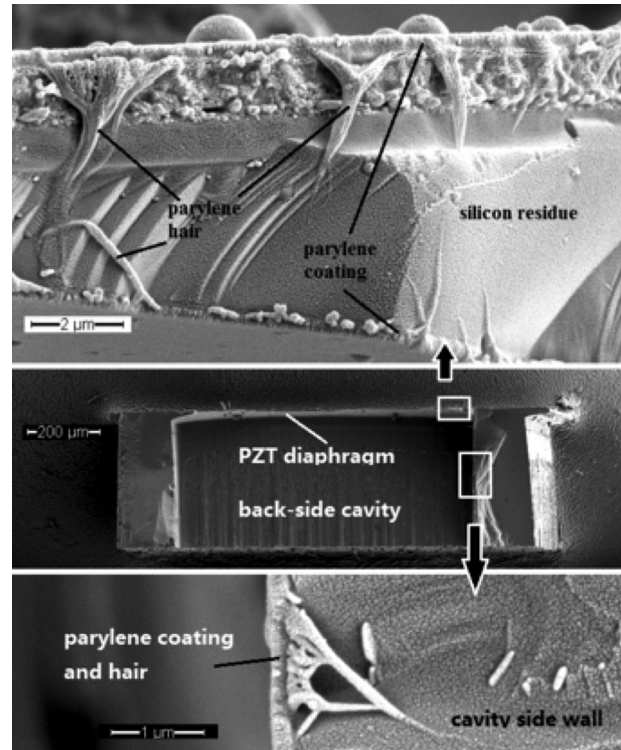| Layer	Material	Thickness (nm)	Density (kg/m^3)
Top	Parylene	250	1110
	Gold	200	19,280
	Chromium	50	7190
	PZT	1000	7500
	Platinum	100	21,450
	Titanium	50	4500
	Nitride	200	3000
	Oxide	500	2650
Bottom	Parylene	250	1110

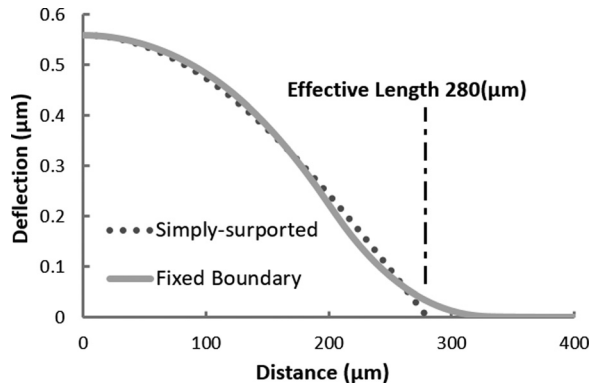**Fig. 6 Cross-sectional view of the probe**

Fig. 7 Deflection profile and equivalent length

diaphragm to a fixed boundary condition. If we extrapolate the half-sine distribution in Fig. 7, we obtain an equivalent length of the PZT diaphragm roughly as $l \approx 560\,\mu m$. With this equivalent length, the model by Yadykin et al. [18] leads to $m_f/m = 26.90$ and $\omega_f \approx 15.1$ kHz, which is closer to the experimental measurement. Similarly, the model by Meyerhoff [19] leads to $m_f = 7.985 \times 10^{-8}$ and $\omega_f \approx 27.4$ kHz, which is higher than the measured natural frequency. As one can see, a slight change in the boundary conditions also leads to a huge variation in the predicted added mass and natural frequency in water.

The third source of discrepancy is uncertainties of the diaphragm mass. Accurate estimate of the diaphragm mass is extremely difficult for a number of reasons. For example, the exact thickness of each layer is difficult to obtain. Under an electronic scanning electron microscope (SEM), the thickness could easily vary by 10% if the layer is not oriented perfectly with respect to the SEM [20]. Moreover, deep reactive ion etch has smaller etching rate at the edges, resulting in nonuniform diaphragm thickness [20] as shown in Fig. 6.

Because of these reasons, we can only estimate the diaphragm mass to the best of our knowledge, and we expect that some inaccuracy may occur. For example, the thickness in Table 1 does not include the silicon residue. Also, the thickness of various layers shown in Table 1 is measured from a similar probe that comes from the same batch and has already been dissected. Although the information from Table 1 is not exact, it should give us a rough estimate of the diaphragm mass.

6 Numerical Studies

From the theoretical analysis above, we can be absolutely sure that the added mass is one order-of-magnitude larger than the diaphragm mass. As a result, the added mass can easily bring the natural frequency from 80 kHz down to the vicinity of 20 kHz. Accuracy of the theoretical analysis, however, is limited due to various assumptions made in the theory. Also, it is not clear if the assumptions are met in the experimental setup. For example, is the water level in the experiment deep enough so that water around the diaphragm can be adequately considered as a half-infinite domain? Do the silicon sidewalls supporting the diaphragm obstruct the flow field affecting the added mass? Does the presence of silicon residue affect the added mass? Answers to these questions and an accurate prediction of the added mass call for a numerical study of the diaphragm–fluid system.

Successful prediction of added mass and its influence on natural frequencies falls into the realm of fluid–structure interaction (FSI), which is still under active investigation. Based on current literature, there are two ways to conduct a numerical study of FSI. The first way is to develop numerical simulations in the structural and fluid domains, respectively, and couple independent solvers, such as finite element method (FEM) and computational fluid dynamics (CFD), via the fluid–structure interface [21–23].

Information computed at each domain is updated and interchanged at each computational step via the fluid–structure interface to ensure certain convergence criteria. For example, Wang et al. [21] numerically modeled the coupled FSI problems by coupling two computational domains together with independent solvers for each domain, passing boundary conditions from each domain to the other at every computational step. To model complex fluid domains, one can employ various CFD solvers such as large-eddy simulations or shear stress transport models to model turbulence. As a tradeoff, it typically consumes large computational resources.

The second approach is to formulate the fluid domain as compressible fluid [24–26]. The formulation is equivalent to lossless acoustic wave equations. The lossless acoustic wave equations and structural equations can be combined into a single set of governing equations and subsequently discretized via FEM. As a result, any commercially available finite element solver, such as ANSYS, can be used. For example, Hengstler [26] employed this approach to consider a fluid domain interacting with an elastic plate. In one of his case studies, the bottom of the fluid domain is coupled with an elastic plate, while the top of the fluid domain is subjected to a free or a fixed (e.g., a wall) boundary condition. This particular case study reveals two marvelous results. First, the free or fixed boundary condition at the top of the fluid domain affects the natural frequency of the plate submerged in the fluid. When the top boundary condition is free, the natural frequency decreases as the depth of the fluid domain increases. In contrast, when the top boundary condition is fixed, the natural frequency increases as the depth of the fluid domain increases. Second, the fluid region that interacts with the plate vibration is limited. When the depth of the fluid domain is large enough, the depth does not affect the fluid–structure interaction significantly.

Having considered the ease and flexibility to conduct the numerical studies, we decide to adopt the second approach and use ANSYS to study the diaphragm–fluid interaction. Two rounds of simulations are performed. The first round of simulations focuses on the influence of water level. The second round of simulations focuses on the influence of sidewalls and silicon residue.

6.1 Influence of Water Level. A finite element model is developed to predict the natural frequencies of the submerged diaphragm with various water levels (see Fig. 8). The model includes two domains: a structure domain (Fig. 8(a)) and a fluid domain (Fig. 8(b)). The structural domain is the diaphragm, and it is submerged in the fluid domain. Only a quarter of the domains are considered and symmetry is used. Table 2 lists the material properties and dimensions of the structure and fluid domains. The structural and fluid domains are explained in detail as follows.
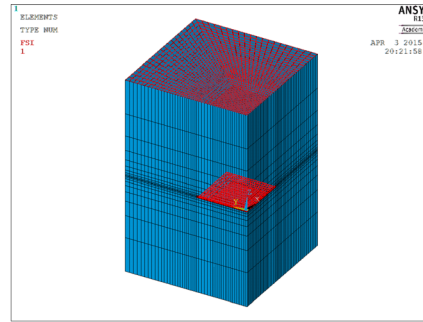
For the structural domain (Fig. 8(a)), its dimensions are identical to a quarter of the diaphragm, i.e., the thickness is $h = 2.6\ \mu m$ and the length is 400 μm. The structural domain is simplified as a square thin plate with isotropic and homogeneous material properties instead of layered. The plate has an averaged density of the diaphragm (cf. Table 1) and has an adjusted Young's modulus such that the first fundamental mode has a natural frequency close to the experimental result (80 kHz). It is discretized using a Solid 186 element, which is a higher-order 3D, 20-node, solid element that exhibits quadratic displacement behavior. Finally, the plate is subjected to a symmetry boundary condition along edges $x = 0$ and $y = 0$ as well as a fixed boundary condition along edges $x = 400$ μm and $y = 400$ μm.

Modeling the structural domain via a homogeneous plate is a simple yet accurate alternative. Theoretically, the factors that affect the added mass are the total mass and mode shape of the structure of interest. A model with layered material properties will not have a significantly different mode shape compared with a homogenous one as long as their natural frequencies are equal.

The fluid domain (Fig. 8(b)) is modeled as water using Fluid 220 element, which is a 3D, 20-node, pressure-based, acoustic
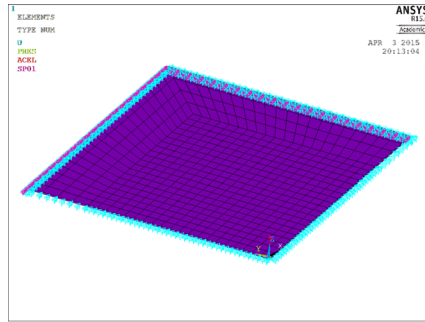
Fig. 8   A quarter finite element model: (*a*) structural domain and (*b*) fluid domain

Table 2   Material properties and dimensions of the fluid–structure model

Domain	Material properties		Dimensions	
Structure (square plate)	Young's modulus (GPa)	250.88	Length/width (μm)	400
	Poisson's ratio	0.33		
	Density (kg/m^3)	6371.3	Thickness h (μm)	2.6
Fluid	Wave speed (m/s)	1460	Area (μm^2)	1000×1000
	Density (kg/m^3)	1000.3	Total water level (μm)	1562.6

element. It is capable of simulating the fluid–structure interaction to study the dynamics of submerged structures [22]. At the fluid–structure interface, the acoustic elements (from the fluid domain) share common nodes with the solid elements (from the structural domain). As a result, there is no need to apply moving mesh techniques at the fluid–structure interface.

Unlike the structure domain, the dimensions of the fluid domain are not so straightforward to determine for several reasons. First, the fluid domain takes substantially more elements to mesh than the structure domain. It is not feasible to model the entire fluid domain encountered in the experiment (cf. Fig. 3). Second, Hengstler [26] has shown that only a limited fluid region will interact with the vibrating structure. Therefore, it is critical to identify a set of suitable dimensions to model the fluid domain. On the one hand, the fluid domain must be large enough to include the entire region where fluid and structure interact. On the other hand, the fluid domain must not be too large to remain computationally feasible.

Guided by these principles, we define the fluid domain via the following steps. First, the fluid domain appears above and below the structure domain (i.e., the square plate) to reflect the experimental setup, in which water appears on both sides of the diaphragm (cf. Fig. 3). Second, the fluid domain is predominant in the out-of-plane direction. Specifically, the fluid domain has an in-plane dimension of 1000 μm, as opposed to 400 μm of the structural domain. This is a ratio of 2.5. In contrast, the fluid domain has an out-of-plane dimension of 1562.6 μm, whereas the structure domain has a thickness of 2.6 μm. This represents a ratio of 601. The fluid domain is chosen this way deliberately, because the displacement of the diaphragm mainly takes place in the out-of-plane direction. As a result, the critical region where the fluid–diaphragm interaction occurs will also be in the out-of-plane direction. Finally, the top surface of the fluid is subjected to a free surface boundary condition while other five surfaces are subjected to wall boundary conditions.

To ensure that the fluid domain is large enough to enclose the critical region of fluid–structure interaction, we conduct the following two numerical trials. In the first trial, the water level above the plate is kept at 780 μm, which is 300 times of the plate thickness h (i.e., 300h). The top surface of the water remains free. In the meantime, the water level under the plate is varied from 130 μm (i.e., 50h) to 780 μm with an increment of 130 μm.
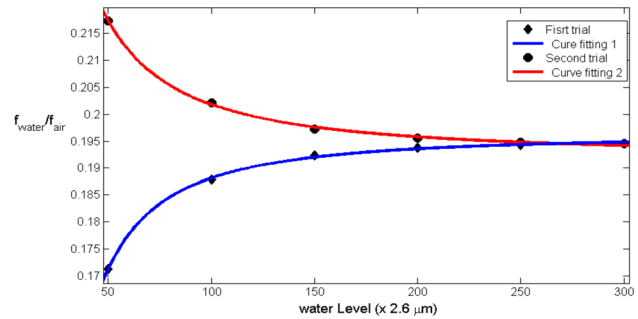

Fig. 9   Ratio of natural frequencies in water and in air as a function of water level

The bottom surface of the water under the plate is fixed. In each numerical run, the natural frequencies and pressure distribution of the fluid–structure system are calculated. Figure 9 shows the ratio of natural frequencies in water and in air as a function of the water level. For the first trial, it shows that the natural frequency increases as the water level below the plate increases, which is consistent with the observation by Hengstler [26].

In the second trial, the arrangement is reversed. The water level below the plate is kept at 780 μm, and the bottom surface of the water is fixed. The water level above the plate is varied from 130 μm (i.e., 50h) to 780 μm with an increment of 130 μm. The top surface of the water above the plate remains free. As shown in Fig. 9, the natural frequency decreases as the water level above the plate increases, which is also consistent with the observation by Hengstler [26].

The simulated results in Fig. 9 also prove that the fluid domain is big enough to enclose the critical region where the fluid–structure interaction takes place. Curve fitting of the calculated data shows that the natural frequencies of each trial follow an exponential form $\mp ax^{-b} + c$, where $a, b, c > 0$. This implies that these natural frequencies are expected to converge to a constant as the water level goes to infinity. Based on the simulated results, the maximal rate of frequency change is less than 0.2 Hz/μm when the water level is in the range of 650–780 μm. This implies that the finite element model will have very good frequency convergence when the water levels on both sides are

780 μm. The fluid domain we define in Table 2 and Fig. 8 does include the critical region of fluid–diaphragm interaction.

Finally, these two trials on water level also justify our choice of theoretical models presented in Sec. 4. Since the water level in the experiments is at least ten times larger than that of the finite element model, the experimental fluid domain behaves like an infinite domain to the vibrating diaphragm.

For the rest of the paper, the fluid–structure model in Sec. 6.1 will be called a "reference model" for convenience. Based on the reference model, the calculated natural frequency of the diaphragm in water is 15.6 kHz, which is 19.5% of the natural

frequency in air (cf. Fig. 9). The calculated natural frequency is very close to the measured natural frequency of 20 kHz in water.

6.2 Influence of Silicon Sidewalls and Residue. In addition to the reference model, we have also built three finite element models to simulate effects of silicon sidewalls and residue. Figure 10 compares the fluid domain and structure domain of these models with respect to the reference model. Specifically, Fig. 10(a) shows the reference model, Fig. 10(b) the diaphragm with silicon sidewalls, Fig. 10(c) the diaphragm with silicon residue, and Fig. 10(d) the diaphragm with the silicon sidewalls and the

(a)　　　　　　　　　　(b)

(c)　　　　　　　　　　(d)
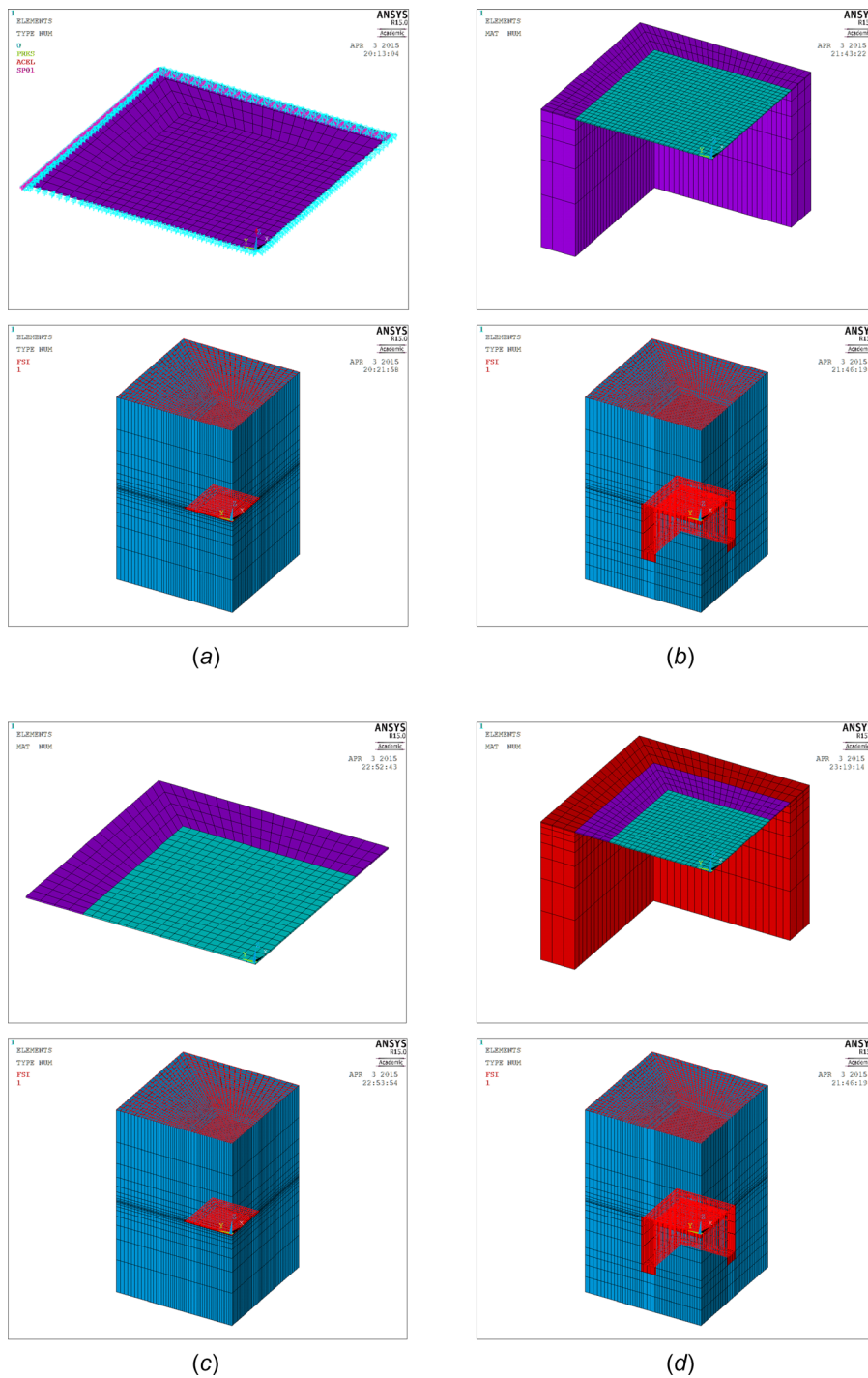
Fig. 10 Fluid–structure finite element models: (a) the reference model, (b) diaphragm with sidewalls, (c) diaphragm with silicon residue, and (d) diaphragm with sidewalls and silicon residue

Table 3 Simulated natural frequencies of four models: (a) reference model, (b) diaphragm with sidewalls, (c) diaphragm with silicon residue, and (d) diaphragm with both sidewalls and residue

Models	Frequency in air (kHz)	Frequency in water, f_{water} (kHz)	Frequency drop (kHz)	Frequency drop %
Reference	80.0	15.6	64.4	80.50
Diaphragm and sidewalls	80.0	16.2	63.8	79.75
Diaphragm and residue	80.0	17.9	62.1	77.63
Diaphragm, sidewalls, and residue	80.0	18.2	61.8	77.25
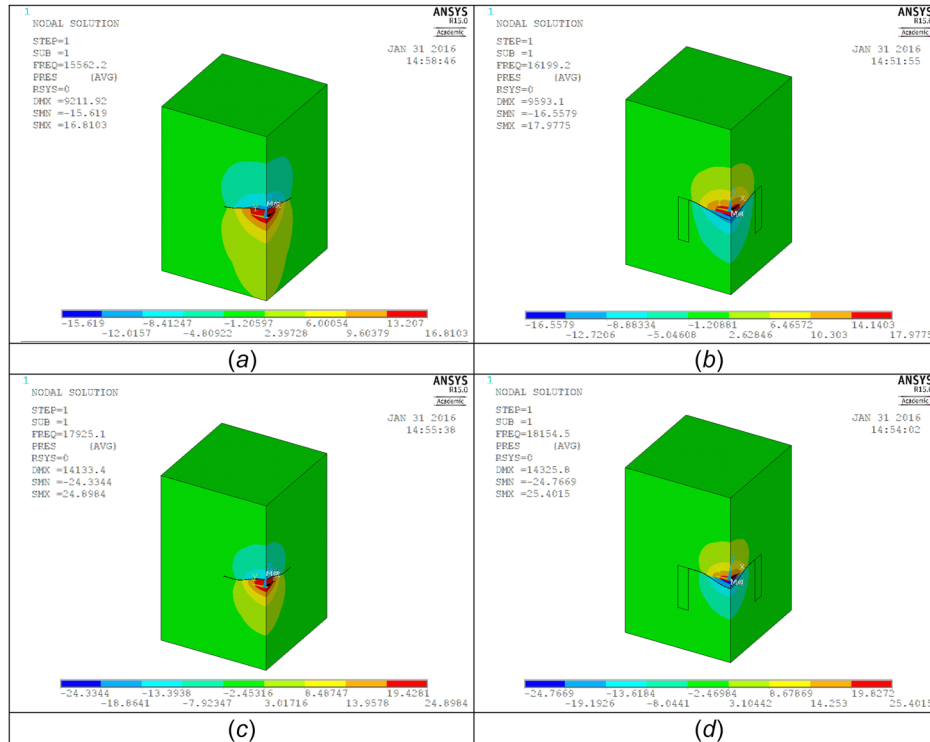
Fig. 11 Simulated pressure field of four models: (*a*) reference model, (*b*) diaphragm with sidewalls, (*c*) diaphragm with silicon residue, and (*d*) diaphragm with both sidewalls and residue

residue. The fluid domain of these models is identical (e.g., dimensions, material properties, and boundary conditions). For each structural domain, its density is identical to that of the reference model. Moreover, the Young's modulus of each structural domain is tuned such that the first natural frequency of each structure in air is identical to that of the reference model (i.e., 80 kHz).

With these models, we study the effects of sidewalls and residue by calculating the first natural frequency and pressure distribution in the fluid domain. In particular, Table 3 compares the natural frequency, whereas Fig. 11 compares the pressure distribution from various models.

Among these calculations, the most insightful one is the pressure field because it allows us to identify the regions of fluid–structure interaction. According to Ref. [26], the influenced fluid region has an effect on the natural frequency. Generally speaking, the more the fluid is influenced, the more the natural frequency is reduced due to increased added mass. The basic idea can be illustrated from the perspective of energy balance. In a fluid–structure interaction problem, the structure initially accelerates the nearby fluid to develop an influenced region. At a steady-state, the region is fully developed. Moreover, the power pumped into the fully developed fluid region must be equal to the rate of change in kinetic energy of the structure. Consequently, the more power is pumped into the fluid, the higher is the rate of change in kinetic energy of the structure, and thus, the lower is the natural frequency.

With the background information provided above, let us now explain these three additional finite element models and their predicted results in detail as follows.

6.2.1 Diaphragm With Sidewalls. The purpose of this model (cf. Fig. 10(*b*)) is to study whether or not the sidewalls have confined motion of the fluid and thus affected the added mass and natural frequency of the diaphragm. The diaphragm size remains 400 μm × 400 μm, and the diaphragm is anchored to the sidewalls at $x = 400$ μm and $y = 400$ μm. Symmetric boundary conditions are applied at $x = 0$ and $y = 0$ as in the reference model. Since the sidewalls are extremely bulky compared with the diaphragm, vibration of the silicon sidewalls is not considered and all degrees-of-freedoms of the sidewalls are fixed.

One can see from Table 3 that the presence of the sidewalls slightly increases the natural frequency from 15.6 kHz in the reference model to 16.2 kHz. This implies that the presence of the sidewalls reduces the added mass. To understand this new phenomenon, we turn to the pressure fields shown in Fig. 11 for an explanation. As can be seen in the reference model (Fig. 11(*a*)), the fluid is free to flow without any obstruction, and it allows a fully developed fluid region. In the out-of-plane direction, the fully developed region extends to the entire water level 780 μm and dies out near the fluid boundaries. This not only justifies the use of the 780-μm water level for the reference model, but is also consistent with the results shown in Fig. 9. In the in-plane

Table 4 Comparison of theoretical predictions and experimental measurements of the first natural frequency in water

Models	Predicted natural frequency (kHz)	Measured natural frequency (kHz)	Percent difference
Yadykin et al. [18]	15.1	20	24.5
Meyerhoff [19]	27.4	20	37.0
FEA (diaphragm)	15.6	20	22.0
FEA (diaphragm and sidewalls)	16.2	20	19.0
FEA (diaphragm and residue)	17.9	20	10.5
FEA (diaphragm, sidewalls, and residue)	18.2	20	9.0

directions, the fully developed fluid region is slightly larger than the square plate defined in the structure model.

When the sidewalls are present in Fig. 11(*b*), the fluid is not allowed to flow outside the square domain. Instead, the fluid is confined to flow downward. As a result, a narrower and shallower fully developed region is developed. The reduction of the fully developed fluid region has caused the added mass to drop and the natural frequency to increase from the reference model. Note that the presence of sidewalls only obstructs the fluid flow at the very outside region, where the pressure gradient and velocity are minimal. Therefore, the change in the added mass and natural frequency from the sidewalls is also tiny.

6.2.2 Diaphragm With Residue. The purpose of this model (cf. Fig. 10(*c*)) is to study how the residue affects the flow field and thus the added mass. For the structural domain, the diaphragm size remains 400 μm $\times$ 400 μm, but it is divided into a central area and an outer area. The central area is bounded by $0 < x < 300$ μm and $0 < y < 300$ μm. It is elastic and free to deform simulating the uniform diaphragm observed in the experiment. The outer area is to mimic the residue. Although the residue is theoretically elastic, its large thickness does not allow it to deform much. This can be seen from Fig. 7; there is almost no displacement at any location whose position is beyond 300 μm from the center of the diaphragm. Therefore, the outer area is subjected to a fixed boundary condition to mimic the effect of the residue. Again, the symmetric boundary conditions are applied at $x = 0$ and $y = 0$ as in the reference model.

According to Table 3, the presence of the residue has a much larger effect than the sidewalls. It increases the natural frequency from 15.6 kHz in the reference model to 17.9 kHz. The significant change is also reflected in the pressure distribution (see Fig. 11(*c*)). Basically, an even narrower and shallower fully developed fluid region is observed. This is very reasonable, because equivalent half-length of the diaphragm area is reduced from 400 μm to 300 μm. According to Eq. (4), the added mass is proportional to the length-to-thickness ratio of the diaphragm. When the half-length is reduced from 400 μm to 300 μm, the added mass should decrease resulting in an increased in the natural frequency.

6.2.3 Diaphragm With Residue and Sidewalls. In this model, we include both the residue and the sidewalls from above. The purpose is to simulate the experimental setup as much as possible. As can be seen in Table 3, adding the sidewalls to the residue only slightly changes the natural frequency. This is rather interesting. By comparing the pressure distribution in Figs. 11(*c*) and 11(*d*), one can see that the fluid region is little changed after the sidewalls are added to the residue. This is because the residue has already caused most of the fully developed region to localize near the center of diaphragm. This leaves very little fully developed region for the sidewalls to modify. As a result, adding the sidewalls to the residue does not significantly change the added masses. Nevertheless, this model best reflects the experimental setup, and it predicts a natural frequency of 18.2 kHz. Note that the predicted natural frequency is very close to the measured natural frequency (20 kHz) within a 10% margin. This shows that our models are reasonably accurate.

As a final remark, the pressure–deflection field shown in Fig. 11 is basically an eigenfunction (virtually a mode shape)

corresponding to the natural frequency of a coupled fluid–structure system. Therefore, the numbers and units shown in Fig. 11 are all normalized and do not carry much physical meaning. For example, the unit of the pressure is 10^6 Pa/kg$^{0.5}$, and it is certainly not a real physical unit. Also, Figs. 11(*a*) and 11(*c*) have a reversed pressure field compared with Figs. 11(*b*) and 11(*d*). The reversion results from a negative sign to the eigenfunction. It can easily be seen from the deflection of the diaphragm. In Figs. 11(*a*) and 11(*c*), the deflection is upward. In Figs. 11(*b*) and 11(*d*), the deflection is downward. Since Fig. 11 shows an eigenfunction of the deflection–pressure field, the most important piece of information is how far the pressure field stretches. The farther the pressure field stretches, the larger the added mass will be present.

7 Conclusions

A PZT thin-film microactuator employing a diaphragm structure could significantly reduce its first natural frequency when submerged in water, thus reducing its frequency bandwidth. Experimental measurements demonstrate such a drop from 80 kHz to 20 kHz. A back-of-the-envelope calculation confirms that the frequency reduction results from the added mass of the surrounding water. The added-mass effect becomes significant, when the length-to-thickness ratio of the diaphragm is large.

Accurate predictions of the frequency drop can be achieved via FEA that simultaneously consider a structural domain and a fluid domain. The FEA indicate that presence of silicon sidewalls and residue surrounding the PZT diaphragm will modify the fluid flow, resulting in a narrower and shallower fully developed fluid region where the fluid and structure interact and exchange energy. Consequently, the presence of the sidewalls and residue leads to smaller added mass and hence a smaller drop in the natural frequency.

Finally, Table 4 summarizes the first natural frequency predicted by two theoretical models and four finite element models. The predicted natural frequencies are also compared with the experimentally measured natural frequency. The natural frequency predicted from the finite element model including all the important features (i.e., the diaphragm, side wall, and silicon residue) has the best agreement with the experimental measurement; the difference is less than 10%.

References

[1] Lee, C. C., Hume, C. R., Cao, G. Z., and Shen, I. Y., 2005, "Development of PZT Thin-Film Microactuators for Hybrid Cochlear Implants," Conference on Implantable Auditory Prostheses, Asilomar, CA, Aug. 1–4.
[2] Lee, C. C., Hume, C. R., Cao, G. Z., and Shen, I. Y., 2005, "A Feasibility Study of PZT Thin-Film Microactuators for Hybrid Cochlear Implants," 27th Annual International Conference of the Engineering in Medicine and Biology Society

(IEEE-EMBS 2005), Shanghai, China, Jan. 17–18, Paper No. 1034, pp. 1929–1932.

[3] Wilson, B. S., Lawson, D. T., Muller, J. M., Tyler, R. S., and Kiefer, J., 2003, "Cochlear Implants: Some Likely Next Steps," Annu. Rev. Biomed. Eng., **5**(1), pp. 207–249.

[4] Gantz, B. J., Turner, C., Gfeller, K. E., and Lowder, M. W., 2005, "Preservation of Hearing in Cochlear Implant Surgery: Advantages of Combined Electrical and Acoustical Speech Processing," Laryngoscope, **115**(5), pp. 796–802.

[5] Dorman, M. F., and Gifford, R. H., 2010, "Combining Acoustic and Electric Stimulation in the Service of Speech Recognition," Int. J. Audiol., **49**(12), pp. 912–919.

[6] Cohen, N., 2007, "The Totally Implantable Cochlear Implant," Ear Hear., **28**(2), pp. 100S–101S.

[7] Briggs, R. J. S., Eder, H. C., Seligman, P. M., Cowan, R. S. C., Plant, K. L., Dalton, J., Money, D. K., and Patrick, J. F., 2008, "Initial Clinical Experience With a Totally Implantable Cochlear Implant Research Device," Otol. Neurotol., **29**(2), pp. 114–119.

[8] Luo, C., Cao, G. Z., and Shen, I. Y., 2013, "Development of a Lead-Zirconate-Titanate (PZT) Thin-Film Microactuator Probe for Intracochlear Applications," Sens. Actuators, A, **201**, pp. 1–9.

[9] Bao, M., and Yang, H., 2007, "Squeeze Film Air Damping in MEMS," Sens. Actuators, A, **136**(1), pp. 3–27.

[10] Pratap, R., Mohite, S., and Pandey, A. K., 2007, "Squeeze Film Effects in MEMS Devices," J. Indian Inst. Sci., **87**(1), pp. 75–94.

[11] Hong, E., Trolier-McKinstry, S., Smith, R., Krishnaswamy, S. V., and Freidhoff, C. B., 2006, "Vibration of Micromachined Circular Piezoelectric Diaphragms," IEEE Trans. Ultrason. Ferroelectr. Freq. Control, **53**(4), pp. 697–706.

[12] Olfatnia, M., Shen, Z., Miao, J. M., Ong, L. S., Xu, T., and Ebrahimi, M., 2011, "Medium Damping Influences on the Resonant Frequency and Quality Factor of Piezoelectric Circular Microdiaphragm Sensors," J. Micromech. Microeng., **21**(4), p. 045002.

[13] Park, K., Shim, J., Solovyeva, V., Corbin, E., Banerjee, S., and Bashir, R., 2012, "Hydrodynamic Loading and Viscous Damping of Patterned Perforations on Microfabricated Resonant Structures," Appl. Phys. Lett., **100**(15), p. 154107.

[14] Luo, C., Cao, G. Z., and Shen, I. Y., 2012, "Enhancing Displacement of Lead-Zirconate-Titanate (PZT) Thin-Film Membrane Microactuators Via a Dual Electrode Design," Sens. Actuators A, **173**(1), pp. 190–196.

[15] Olfatnia, M., Singh, V. R., Xu, T., Miao, J. M., and Ong, L. S., 2010, "Analysis of the Vibration Modes of Piezoelectric Circular Microdiaphragms," J. Micromech. Microeng., **20**(8), p. 085013.

[16] Dahl, D., Kleinschmidt, E.-G., and Vick, U., 1977, "Determination of the Perilymph Density in the Cochlea of Guinea Pigs," Arch. Oto-Rhino-Laryngol., **215**(3), pp. 339–341.

[17] Koshigoe, S., Kwok, W.-K., and Tubis, A., 1983, "Effects of Perilymph Viscosity on Low-Frequency Intracochlear Pressures and the Cochlear Input Impedance of the Cat," J. Acoust. Soc. Am., **74**(2), pp. 486–492.

[18] Yadykin, Y., Tenetov, V., and Levin, D., 2003, "The Added Mass of a Flexible Plate Oscillating in a Fluid," J. Fluids Struct., **17**(1), pp. 115–123.

[19] Meyerhoff, W. K., 1970, "Added Masses of Thin Rectangular Plates Calculated From Potential Theory," J. Ship Res., **14**(2), pp. 100–111.

[20] Lee, C.-C., Cao, G. Z., and Shen, I. Y., 2010, "Effects of Residual Stresses on Lead–Zirconate–Titanate (PZT) Thin-Film Membrane Microactuators," Sens. Actuators A, **159**(1), pp. 88–95.

[21] Wang, W. Q., He, X. Q., Zhang, L. X., Liew, K. M., and Guo, Y., 2009, "Strongly Coupled Simulation of Fluid–Structure Interaction in a Francis Hydroturbine," Int. J. Numer. Methods Fluids, **60**(5), pp. 515–538.

[22] Munch, C., Ausoni, P., Braun, O., Farhat, M., and Avellan, F., 2010, "Fluid–Structure Coupling for an Oscillating Hydrofoil," J. Fluids Struct., **26**(6), pp. 1018–1033.

[23] Liaghat, T., Guibault, F., Allenbach, L., and Nennemann, B., 2014, "Two-Way Fluid–Structure Coupling in Vibration and Damping Analysis of an Oscillating Hydrofoil," ASME Paper No. IMECE2014-38441.

[24] Jhung, M., Choi, Y., and Jeong, K., 2003, "Fluid Bounding Effect on Natural Frequencies of Fluid-Coupled Circular Plates," J. Mech. Sci. Technol., **17**(9), pp. 1297–1315.

[25] Liang, Q. W., Rodriguez, C. G., Egusquiza, E., Escaler, X., Frahat, M., and Avellan, F., 2007, "Numerical Simulation of Fluid Added Mass Effect on a Francis Turbine Runner," Comput. Fluids, **36**(6), pp. 1106–1118.

[26] Hengstler, J. A. N., 2013, "Influence of the Fluid–Structure Interaction on the Vibrations of Structures," Ph.D. dissertation, ETH Zürich, Zürich, Switzerland.